Microscale Templating of Functional Particles using Self-Limiting Electrospray Deposition

Michael J. Grzenda[1]*, Jouan Yu*[1]*, Maria Atzampou*[2]*, Christopher E. Shuck*[3]*, Yury Gogotsi*[4]*,*
Jeffrey D. Zahn[2]*, Jonathan P. Singer*[1]

1. Department of Mechanical and Aerospace Engineering, Rutgers University, Piscataway, New Jersey 08854, USA. E-mail: jonathan.singer@rutgers.edu
2. Department of Biomedical Engineering, Rutgers University, Piscataway, NJ 08854, USA
3. Department of Chemistry and Chemical Biology, Rutgers University, Piscataway, NJ 08854, USA
4. A.J. Drexel Nanomaterials Institute, and Department of Materials Science and Engineering, Drexel University, Philadelphia, Pennsylvania 19104, USA

Abstract

Electrospray deposition (ESD) uses strong electric fields applied to solutions and dispersions exiting a capillary to produce charged monodisperse droplets driven toward grounded targets. Self-limiting electrospray deposition (SLED) is a phenomenon recently developed by our group in which highly directed, uniform, and even three-dimensional coatings can be achieved by trapping charge in the deposited film, redirecting the field lines to uncoated regions of the target. However, when inorganic particles are added to SLED sprays, the buildup of charge required to repel incoming material is disrupted as particle loading increases. Due to its fibril gelling behavior, methylcellulose (MC) SLED can form nanowire morphologies due to its fibril gelling behavior. These wires, when used as a binder, can separate particles and prevent percolation. In this work, we explore a variety of conductive and insulating particles using patterned and un-patterned substrates. This exploration allows us to maximally load particles for high-concentration and highly controlled self-limiting functional sprays. This is demonstrated using $Ti_3C_2T_x$ MXene to functionalize an interdigitated electrode for use as a supercapacitor.

1 Introduction

Electrospray deposition (ESD) provides several advantages over more conventional coating methods, such as low cost, high efficiency, ambient spray conditions, electric field-directed deposition, and the ability to produce hierarchical structures and complex surface morphology. Our group has recently classified electrospray regimes while demonstrating the self-limiting (SL) regime.[1] These regimes depend on the sprayed material's dielectric behavior, crystallinity, and mobility (e.g., glass transition behavior). In electrowetting and charged melt regime sprays, the growing films can rearrange themselves to dissipate charge. By contrast, in self-limiting electrospray deposition (SLED), the charge is trapped in the growing film, which eventually causes the spray to redirect towards uncoated regions of the substrate.[1] This allows for high control over uniformity and can produce 3D coatings.[1, 2] Recently, we compared the three electrospray regimes while targeting 2D conductive test patterns on insulating substrates and demonstrated that the SL regime outperforms the other two in both spray fidelity and uniformity in a model polymer (polystyrene).[3]

Nevertheless, the compatibility of electrospray with nanoparticles[4, 5] and flexible films[6] makes SLED an excellent platform for upgrading and functionalizing 2D devices. Other techniques exist for printed device fabrication, such as inkjet printing,[7-11] gravure printing, screen printing, and conventional spray with masking,[12] but SLED has the added advantages of surface morphology control, non-planar target compatibility, and the potential for near 100% deposition efficiency.[13] Conventional ESD has been employed to create functional devices[14-16] and patterns,[17-19] resulting in a naturally parabolic film and pure particles eventually forming fractal structures.[20] Researchers have tried to counteract these effects using larger spray areas[21], which can be wasteful, or a focusing printhead.[22] These strategies are less effective when targeting 3D objects or complex 2D templates.

Adding nanoparticles to SLED sprays poses an obvious challenge. When conductive particles are added to a dielectric matrix, the bulk conductivity of the composite increases, so the deposited film will not maintain the charge capture needed for SL behavior. While particles initially cause little change in bulk electrical properties, once the percolation threshold is reached, changes can occur by orders of magnitude.[23] By contrast, semiconducting and dielectric particles will likely not experience a percolation threshold. However, work by Zhu and Chiarot showed semiconducting TiO_2 particles experiencing growing fractal networks, similar to conductive particles, both as films[24] and when combined with a near-field template, which contrasts the filling and termination of a SLED polymer.[20] Even for dielectric particles, we expect non-SLED behavior to be the norm due to the surface wetting of the carrier solvent. However, we have found that SL and non-SL materials can produce SL blends at certain ratios.[25] Therefore, the addition of particles to SLED sprays will likely depend on (i) the concentration and (ii) the type of particle, as well as (iii) the SLED binder morphological evolution.

Our work with methylcellulose (MC) has shown that in ESD, MC solution droplets can evolve into nanowires, eventually leading to SL nanowire forests and foams.[26] We hypothesize that this high-aspect ratio insulation is ideal for preventing percolation at low polymer volumes. Indeed, it was further demonstrated that SLED forests could be deposited with small loadings (~3 vol%) of polymer-capped gold nanoparticles, maintaining their single-particle plasmon in a three-dimensional coating. Further work, via simulation and experimentation, showed that adding particles modifies solution viscosity, impacting nanowire formation and, ultimately, the deposited film.[27] More specifically, large spherical particles (>200 nm) suppress nanowire formation while smaller particles (<70 nm) are incorporated. In this smaller regime, the particle-to-MC ratio controls the nanowire's length, with excessive loading inhibiting wire formation. It was also seen that sharp-edged particles focus the electric field, leading to the formation of nanowires at these vertices, even for larger particles. While insight was gained on the self-assembly of composite ESD droplets, it was not evaluated if the macroassemblies of these composites were in the SL regime, and the properties of these macroassemblies were not evaluated. It remains unknown to what extent functional nanoparticles can be loaded into a SL binder while maintaining the advantages of SLED for 2D microelectrodes[3] and 3D topologies.[28] The main goal of maximizing particle loading is to employ the deposits as "green bodies," with binder burnt off to increase the active fraction and percolation of the final structure and enable functional devices. We have previously established a rough limit of ~30% non-SL material in soft matter blends,[25] but these possess completely different percolation behavior that arises from micro/macrophase separation during solvent evaporation. Further, none of the non-SL materials examined in our past work were electrically conductive, meaning that the dissipation was all mass transport driven, which is not the case in many particle composites, including several described below.

To establish these limits, we use 2D $Ti_3C_2T_x$ MXene of two different sizes as well as 0D ITO (65 nm), silver (15 nm), titanium (70 nm), and silica (22 nm) nanoparticles incorporated into MC composite sprays. The growth of these films at various particle loadings was studied on 2D test pattern templates. By optimizing the particle loading, we achieved highly controlled sprays with particle loadings an order of magnitude greater than we had previously explored, allowing us to upgrade a 2D interdigitated electrode with MXene for use as a supercapacitor through the burning of the MC binder.

2 Materials and Methods

2.1 Materials

Substrate materials included p-type Si wafers (0-100 Ω-cm) purchased from University Wafer, Inc.; gold interdigitated electrodes (IDE) on boro-aluminosilicate glass purchased from Platypus Technologies; and Ti/Pt test patterns were fabricated in-house on Si as described previously[3] with unpatterned areas insulated with 4-5 μm thick Parylene. These patterns were designed with 1 mm long rectangular features that varied in width (20, 30, 60, 120, 240 μm) and spacing as a function of width (0.33x, 1x, 2x, 3x, 9x). The 30 μm feature/270 μm gap grating was chosen to compare the performance of different materials on a small feature. 30 μm features were selected from over 20 μm because the largest gap found on a 20 μm feature is 180 μm, making it more prone to saturation.

Methylcellulose (15 cP) was used as received from Sigma Aldrich. Aqueous particle dispersions were obtained from various suppliers: the ITO dispersion was purchased from NYACOL® Nano Technologies, Inc. (64 nm particle size; 20 wt.%); the silver (15 nm; 5 wt.%) and titanium (70 nm; 15 wt.%) were purchased from US Research Nanomaterials, Inc.; LUDOX® TM-50 colloidal silica solution (22 nm; 50 wt.%) was purchased from Sigma Aldrich; and $Ti_3C_2T_x$ MXene was prepared by etching Ti_3AlC_2 (Carbon Ukraine, <40 μm) in a mixture of HF (Acros International, 49 wt. %), HCl (Fisher Scientific, 12.1 M), and deionized water (DI; 15 MΩ resistance) at an etchant volumetric ratio of 2:6:12 $HF:H_2O:HCl$, as described previously.[29] After washing, the neutral $Ti_3C_2T_x$ was added to 20 mL DI water, and then 1 g LiCl (99%, Alfa Aesar) was added to delaminate the MXene. This was stirred at 300 rpm for 24 h at 35 °C. The MXene was then collected by centrifugation at 3,500 rpm for 15 min, followed by a consequent concentration of 2 wt.% by centrifuging the collected $Ti_3C_2T_x$ at 10,000 rpm for 10 min. To make the spray solutions, MC was mixed directly into the aqueous particle dispersion or DI water and left to fully dissolve overnight. To reduce the size of the MXene particles, sonication was undertaken using a Q500 ultrasonicator with a 1/8” tapered microtip (20 minutes; 20% amplitude; 8:2 pulse). During sonication, 1 ml of MXene dispersion or MXene-MC aqueous solution was added to a 1.5 ml centrifuge tube and suspended in an ice bath to prevent degradation of the MXene. To achieve stable electrospray for all compositions, ethanol was mixed with the aqueous solutions/dispersions at a ratio of 3:2 w/w water to ethanol. The MC concentration was kept at either 1% or 0.25% by weight with respect to the water-ethanol mixture. Particles were sprayed both with and without MC. The various particle concentrations were achieved by diluting the particle-MC solutions with pure MC solutions of equivalent concentration at varying ratios (6.25, 12.5, 25, 50, and 100% dispersion concentration). Percentage volume data is presented in this work considering only the composition of the deposited material, meaning the volume ratio of MC to particles after solvent evaporation. These percentages were calculated from bulk densities for all materials.

2.2 Spray Conditions

The electrospray setup used has been described previously.[1] Briefly, the solution is delivered via a syringe pump with the solution in a disposable syringe (1 mL NORM-JECT®) connected by PTFE tubing to a steel needle (Sai Infusion, 20 gauge, 1.5"). High voltage power supplies (Matsusada Precision Inc. RB30-30P) apply voltage to the steel needle and a steel stabilizing ring (inner diameter of 2 cm and an outer diameter of 4 cm) located 1 cm above the needle tip. Targets are located vertically below the spray needle and are grounded via an alligator clip.

During the spray, the voltage applied to the needle was 6 - 7 kV. The ring voltage varied from 1.8 to 3.1 kV to maintain stable Taylor-cone jet sprays. Ambient humidity ranged from 30 - 60% while temperatures remained between 19 and 22 °C, and the substrate was kept at 90 °C using a hotplate unless specified. The spray distance was maintained at 6 cm, and the material was delivered at a flow rate of 0.1 ml/h. The spray was first stabilized with a 4-inch diameter Si wafer as a target during the experiments. To collect the sample for SEM imaging and thickness measurements, small pieces of Si wafer (~1-3 cm^2) were placed on the larger wafer for varying amounts of time. For patterned materials, the test patterns were grounded to a smaller Si wafer using carbon tape and placed on top of the larger wafer. The test patterns were sprayed with 1% MC solutions for 2 h or 0.25% MC for 8 hours to maintain a constant mass of MC delivered. The

IDE was sprayed with a 28 vol.% MXene-composite for 15 min in a low humidity chamber (20%) at room temperature.

2.3 Characterization

Test patterns were imaged using a Leica DM2700 optical microscope, and the width of the features was measured using ImageJ. Each feature in every grating was measured 3 times at ¼, ½, and ¾ of its length. For comparison across feature sizes, we define a metric, excess width (EW), given by:

$$EW = w_m - w_f, \tag{1}$$

where w_f is the actual width of the feature, and w_m is the measured width after spray. For SL material, we expect all substrate surfaces to coat uniformly, giving a uniform EW regardless of feature size.[3] For film thickness measurements, Si chips were fractured and mounted vertically to allow cross-section imaging. The thickness of the cross sections was measured using a recently published MATLAB script.[30] Materials are graphed as a function of the total solids volume of the material deposited. In previous results, reflectometry measurements of densified films were used to demonstrate that self-limiting materials produce a plateauing thickness over time.[1] However, the films measured here were not densified because the particles prevent thermal or solvent vapor densification. Samples were also viewed using a Zeiss Sigma Field Emission scanning electron microscope (SEM) using both in-lens and backscattering imaging, depending on the contrast provided by the materials.

Electrochemical testing was performed using a Gamry Reference 600+ with a MXene-functionalized IDE submerged in 2M H_2SO_4. A commercially supplied, interdigitated gold electrode (50 μm features/50 μm spacing) was sprayed and thermally post-treated. Microscopy images show that the device was successfully functionalized without shorting, and the MXene maintained a porous morphology after burning. Cyclic voltammetry scans were made between 0 and 6 V at varying rates. Galvanostatic charge/discharge (GCD) experiments were used to calculate the capacitance of the device using the equation:

$$C = \frac{2I}{A(\Delta V)} \int_{t_0}^{t} V dt \tag{2}$$

where I is the current, A is the pattern area, and V is the voltage.

3 Results

3.1 Test Patterns

3.1.1 Sprays of unmixed materials

Materials were sprayed onto conductor-on-insulator test pattern gratings that varied in feature size and spacing. To illustrate the challenges presented by templated ESD of conductive particles, **Figure 1** shows characteristic test patterns sprayed with pure MC, MXene (large), sonicated MXene (small), ITO, and small MXene-MC composite. As a SL material, MC can target the test pattern features with high uniformity and fidelity. In contrast, large MXene flakes deposit in a more disordered fashion, favoring the pattern edges due to focusing from the insulation. The small MXene flakes perform better, possibly due to the higher packing density and increased total resistance due to the number of interfaces. However, the deposition is still highly fractal (low density and non-uniform feature edges). Large areas also show gradients, like the grounding pad seen in **Figure S1**. The pure ITO spray was unstable even when the flow rate was reduced to 0.05 ml/h to compensate. However, despite the low flow rate and instabilities, the particles are focused on the grating edges, which leads to bridging at low levels of material delivery. By contrast, an exemplary result of the small MXene composite spray in the SLED regime reproduces the MC result, albeit with slightly increased EW.

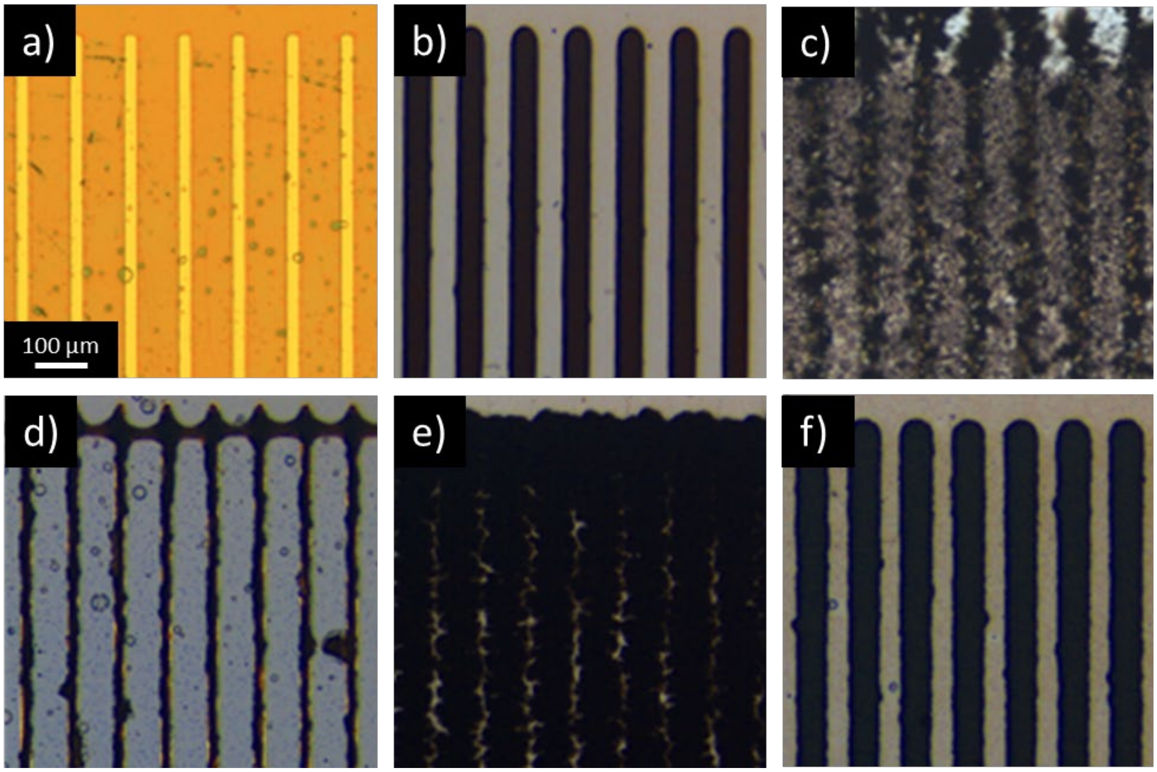

Figure 1. 20 µm grating test patterns (a) uncoated and coated with non-composite sprays of (b) pure MC, (c) large MXene flakes, (d) ITO, (e) small MXene flakes, and (f) the MC composite spray of 28 vol.% small MXene. All figures are at the same scale.

3.1.2 Composite Materials

Silica, large MXene flakes, silver, titanium, and ITO particles were sprayed with 1 wt.% MC solutions, while small MXene was sprayed from both 0.25 and 1 wt.% MC solutions with the amount of MC deposited held constant (2 and 8 h sprays, respectively). The lower concentration of MC was used to spray higher MXene/MC ratios while maintaining spray stability. EW on a 30 µm grating for all the materials sprayed is displayed in **Figure 2**.

Overall, insulating particles like silica show a slight decrease in EW followed by an eventual increase at higher loadings. This behavior is consistent with prior results, which showed a decrease in nanowire length with increased particle loading,[27] though eventually, this effect is counteracted by a reduction in SL behavior, leading to greater material deposition. In contrast, conductive particles show behavior consistent with percolation: Initially, EW increases slightly with particle loading, sometimes experiencing a plateau in EW until a certain threshold is reached, and after EW increases drastically. This threshold is achieved rapidly for silver, followed by large MXene flakes and, finally, small dilute MXene flakes. The highest loading for these particles in the low growth regime is <1 vol.%, 4.7%, and 28%, respectively. Non-dilute small MXene and ITO appear not to percolate in the regimes shown here. Comparing the dilute and non-dilute small MXene, the longer dilute sprays had greater EWs than their composition-matched counterparts. This discrepancy is discussed further in the SI. As will be discussed, titanium behaves similarly to silica, which we expect to be the norm for metallic particles.

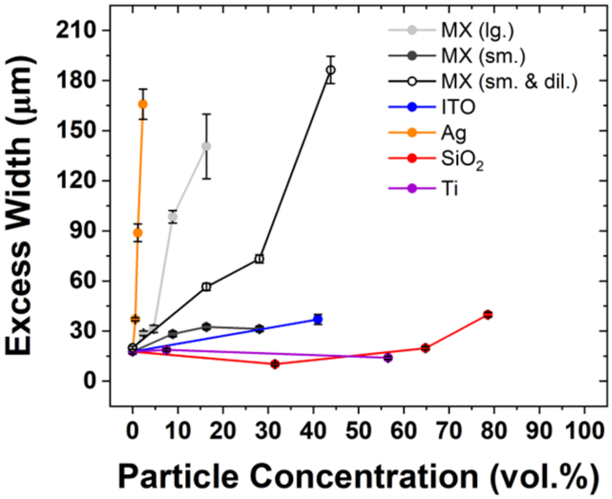

Figure 2. Excess widths of the 30 μm features for all sprayed materials. All composites were sprayed from a solution of 1 wt.% MC for 2 h except for MXene (small and dilute), which was sprayed from 0.25% MC for 8 h. Error bars were calculated by taking the standard deviation of all the features in a gradient.

Table 1. Description of particles dispersed in MC solutions and sprayed onto test patterns.

Particle	Spray Solution	Excess width spray time (hr)	Shape	Log10 Resistivity (Ω-m)	Particle Size (nm)	Surface
MXene - large	1% MC	2	Flake	-6(31)	>1000	Conductive 2D particle
MXene - small	1% MC	2	Flake	-6(31)	<1000	Conductive 2D particle
MXene - small & dilute	0.25% MC	8	Flake	-6(31)	<1000	Conductive 2D particle
ITO	1% MC	2	Round	-6(32)	65	Conductive oxide
Silver	1% MC	2	Round	-7.8(33)	15	Likely no oxide
Silica	1% MC	2	Round	16(34)	22	Insulating oxide
Titanium	1% MC	2	Round	-6.4(33)	70	Likely insulating oxide

3.2 Cross-sectional thickness

Figure 3 shows cross-sectional thickness measurements. Looking solely at the porous MC spray, the plateau behavior is not immediately apparent. However, **Figure S2** shows that the densified thicknesses of these films, measured via reflectometry, rapidly plateaus, indicating that the porosity of the MC increases with thickness. We also see that the non-dilute 28 vol.% MXene films grow at a similar rate to the pure MC films (**Figure 3**). Although films deposited from the dilute 28 vol.% MXene solution are thicker than their non-dilute counterparts, this correlates to the observed EW results in the prior section. Significantly, the 43 vol.% MXene unpatterned film contrasts these results (**Figure S2**), showing a greater initial slope, no indication of plateau behavior, and greater variability as the thickness increases. Interestingly, for all these materials, the EWs on the test patterns are similar to the unpatterned spray thicknesses (**Table S1**), indicating that growth occurs at a similar rate under both conditions. The slight discrepancy may be due to focusing from the surrounding mask increasing the material deposition rate on the test patterns.

The low aspect ratio particles are graphed separately from the MXene particles in **Figure 3b** because the spherical particles can pack more densely than flake-like particles during electrospray. Here, we can draw an interesting contrast from pure SiO_2 spray. Despite being an insulator with nanowire formation, this film has a greater slope than the other low aspect ratio composite sprays. While a longer spray time (17.5 h) was required due to stability issues at higher loadings, a lack of charge build-up appears to dominate deposition. By contrast, all the MC-containing composites have lower slopes and seem to aggregate, indicating that built-up charge plays a significant role in the film growth. This is interesting because all of these composites have different particle sizes and loadings, meaning that the nanowire aspect ratios of the composite particles will vary.

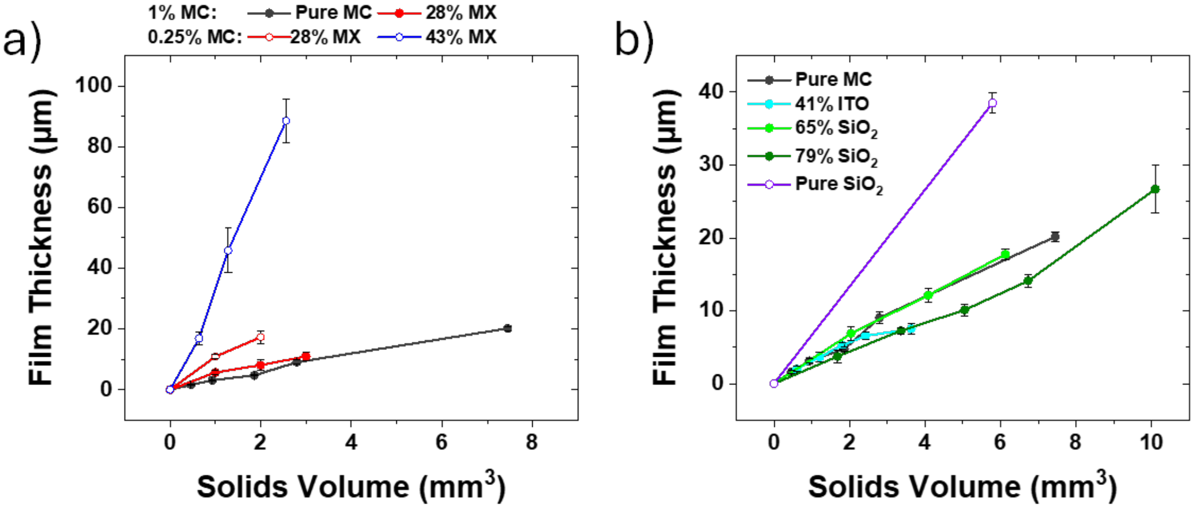

Figure 3. Film thickness measurements of unpatterned substrates by the total solids volume sprayed. (a) 2D MXene materials and (b) 0D particles. The percentages next to the particle labels indicate the volume ratio of solids after deposition relative to MC.

3.3 Deposition Morphology

Several compositions were also imaged using SEM to demonstrate spray morphology. The pure MC nanowires are shown in **Figure 4a.** As demonstrated by work with silica, the concentration of small particles controls nanowire length,[27] which can be seen here with ITO particles. At 40.6 vol.%, ITO maintains the nanowire morphology (**Figure 4b**) even after burning, with fine features still intact **(Figure 4c**). At higher concentrations, the ITO nanowires form ovoid shapes (**Figure 4e**), with MC tails removed after burning (**Figure 4f**). For large MXene flakes, we previously saw that nanowires form at sharp particle edges.[27] By contrast, few nanowires can be seen at 28 vol.% for the small flakes, likely due to the high loading (**Figure 4g**). However, the highly controlled deposition of this composite indicates that MC encapsulates the particle edges. After burning, some collapse can be observed, but a high degree of porosity is clearly maintained.

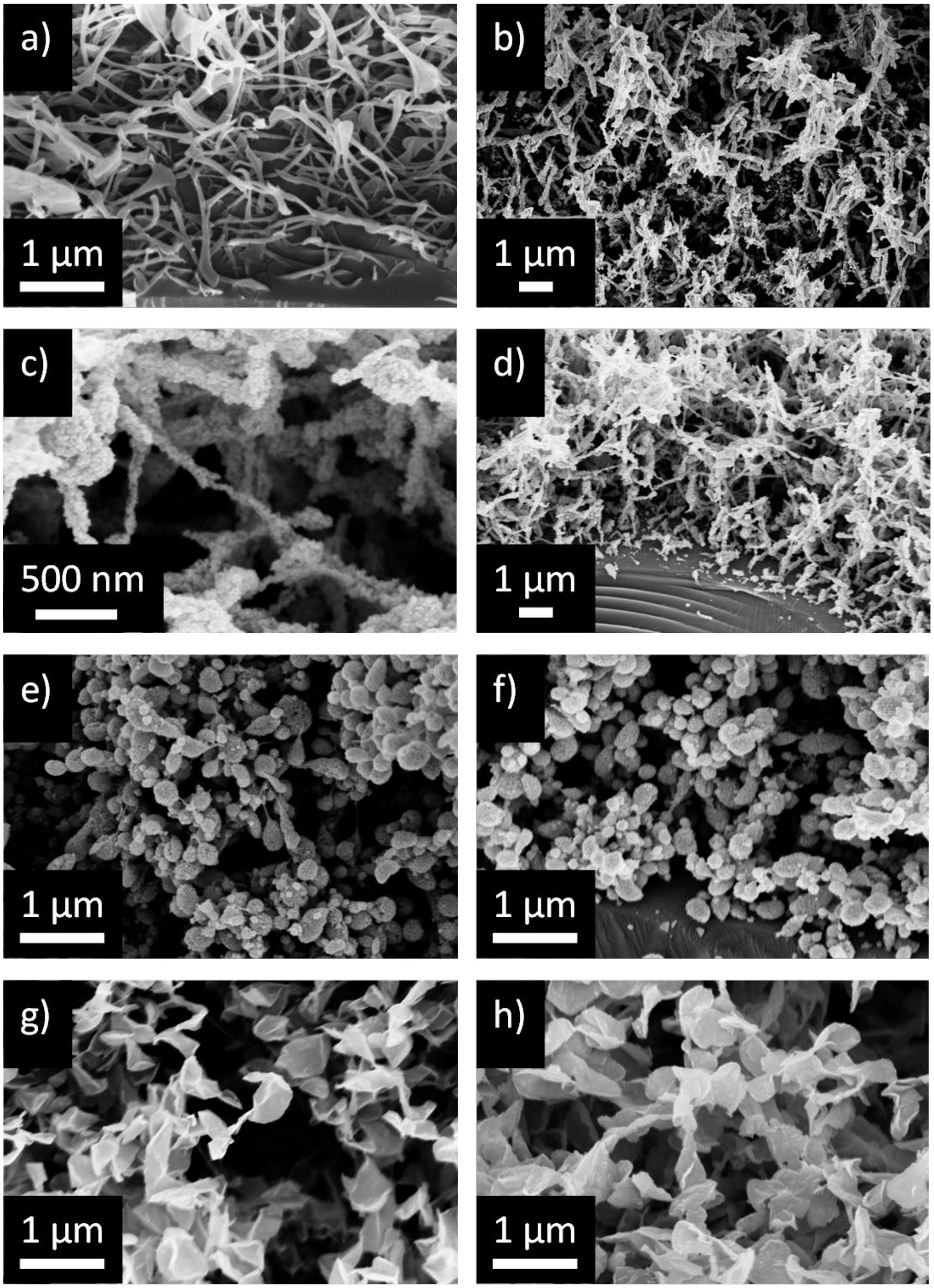

Figure 4. SEM images of (a) pure MC from 1 wt.% solution; 40.6 vol.% ITO from 1 wt.% MC before (b) and after burning (c & d); 84.5 vol.% ITO from 0.25 wt.% MC before (e) and after burning (f); 28 vol.% MXene from 1 wt.% MC before (g) and after burning (h).

3.4 Electrochemical testing

The porosity, seen for all the particles after burning, makes materials deposited via MC composites excellent candidates for electrochemical devices and gas sensors that require large accessible surface area. This was tested using the 28% MXene composites with the electrode shown in **Figure 5a**. Cyclic voltammetry curves show an enormous change in electrochemical behavior compared to an unfunctionalized device with the control demonstrating essentially no response (**Figure 5b**). Simply comparing the hysteresis, the functionalized 200 mV/s data has an area between the curves that is over 450 times greater (**Figure 5c).** The GCD data gives capacities ranging from 0.72 - 1.76 mF/cm^2 for currents ranging from 0.27 – 0.81 mA/ cm^2.

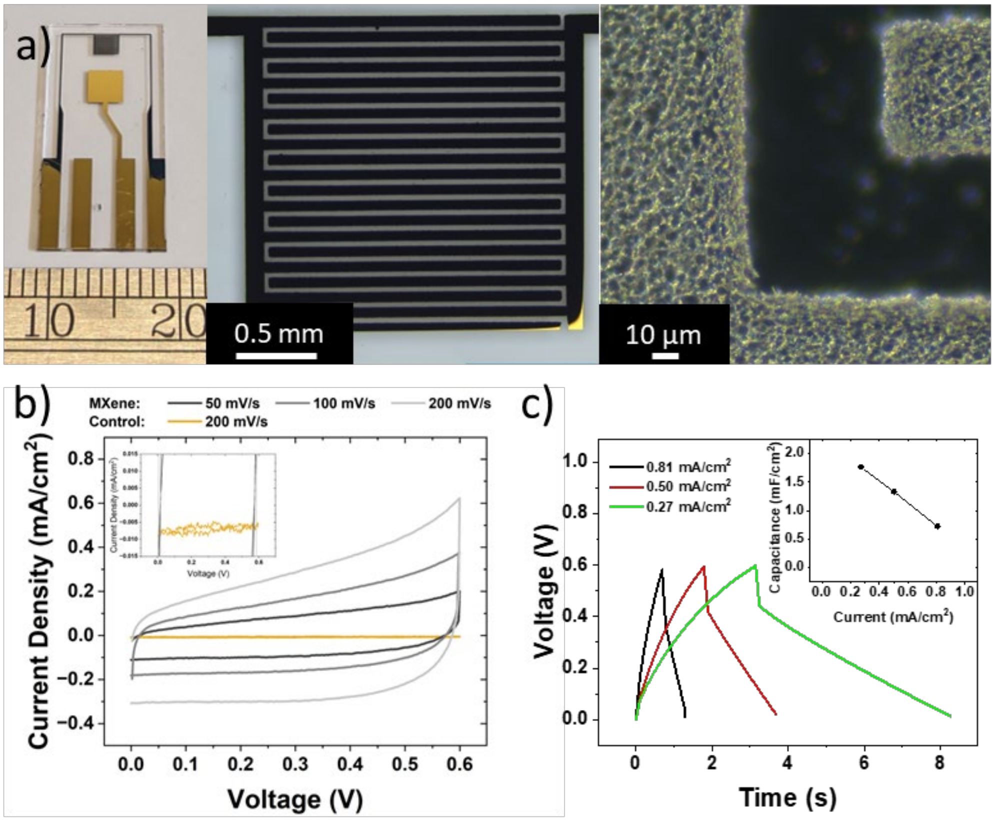

Figure 5. (a) The interdigitated electrode on glass at increasing magnifications with the ruler on the far left in units of mm. (b) Cyclic voltammetry scans and (c) Galvanostatic charge/discharge scans with corresponding capacitance (inset).

4 Discussion

4.1 Effect of particle composition

The electrical properties of the particle and particle solution significantly impact the regime of deposition of the composite film. Silver is the most drastic example of this. Despite having the lowest resistivity, silver nanoparticle sprays displayed percolation-like behavior well below where expected (see **Figure S4** for greater detail). This may have more to do with the behavior of silver in solution than the resistivity of the composite, as seen in the conductivity measurements of the spray solutions (**Figure S5**). This is consistent with past reports that indicate equilibrium between nanoparticulate silver and dissolved silver ions once absorbed oxygen triggers oxidation.[35] Therefore, these ions likely lead to the sharp increase in EW seen for the silver particles.

For silica, we see the opposite behavior. While we can have confidence that the initial reduction in EW is due to a shortening of the nanowires within the SL regime, it is unclear whether the 79 vol.% is still SL. Our previous work with these test patterns showed that the film thickness on features depended more on feature size for non-SL sprays, similar to the EW of 79% silica (discussed in SI). However, when comparing the unpatterned spray thickness of the 79% composite to the pure silica spray, we see that there is a significant difference in the film's rate of growth, with the pure silica growing at a rate of 6.65 $\mu m/mm^3$ and the composite averaging 2.55 $\mu m/mm^3$ trending below the other materials in **Figure 3b** (Pure MC, ITO, and lower silica loadings). While we conventionally define SLED by a plateauing thickness over time, it is also likely that sprays in the SL regime grow at slower rates. As mentioned earlier, for the MC spray, we know that the porosity can change over time, so the original definition is not definitive here. The most likely answer is that SL behavior exists on a spectrum and that the 79% composition is distinctly less SL than the other materials, but the MC still has an important effect on the film's growth.

The EW of titanium composites trended similarly to the silica materials, particle's core being moderately more conductive than ITO. We attribute this to the native dielectric oxide of titanium (expected to be ~3 nm thick)[36] being less conductive than ITO. Simply drop-casting the nanoparticles as a film leads to a measurable conductivity. This result aligns well with the principle of percolation and would suggest that the addition of the oxide layer to the titanium nanoparticles is enough to prevent tunneling when the MC increases the interparticle spacing, allowing charge to accumulate in the growing film.

4.2 Effect of aspect ratio on semi-conducting composites

For the MXene and ITO particles, all having resistivity on the order of 10^{-6} Ω-m, we can make more direct comparisons on the effects of particle aspect ratio. Literature on percolation demonstrates that higher aspect ratio particles percolate more quickly than lower aspect one, with the extreme case being an infinitely long particle.[37] This work shows that the large MXene flakes, with the largest aspect ratio, show a percolation transition at 4.7 vol.%. EWs prior to this transition tend to all be very similar regardless of feature size, indicating a uniform growth rate consistent with SLED behavior. While the composites have slightly increased EW compared to MC, this is not particularly surprising: Adding 2D particles would certainly change the particle packing and MXene also adds non-insulating volume. Above 4.7 vol.%, the EW greatly increases, and we also see a much larger variation in EW strongly dependent on feature size **(Figure S6)**. While larger features trend closer to linear, smaller features show a larger transition, consistent with prior work on non-SLED sprays.[3] Interestingly, the current results differ slightly in the type of non-SLED coating. In the prior work, the non-SLED material was above its glass transition and could dissipate charge due to its higher *mass*-transport mobility.[3] Here, the high-concentration sprays would have equal or lesser mobility to the SLED spray, experiencing continuous fractal growth. However, this does not appear to impact the general trend in this case.

For small MXene flakes at low loadings, the resulting sprays were similar to large flakes, indicating a charge-trapping mechanism in both films. However, the small and large flake composites deviate beyond 4.7 vol.%, with the small MXene EWs plateauing up to 28 vol.%. As we observed in the SEM images (**Figure 4g**), by 28 vol.%, few visible nanowires are present. Therefore, the plateau effect may occur because fewer nanowires hold particles apart, leading to a denser coating or because charge repulsion completely dominates the film growth. In any case, turning to the unpatterned film thickness for the 28% composition, the reduced slope after a volume of 1 mm^3 is deposited strongly suggests that these materials are still in the SL regime.

Despite the increases in EW for the dilute small MXene (discussed in the SI), the trend for dilute and non-dilute small MXene composites is still similar, up to 28 vol.%. After that point, a drastic increase in EW is seen at 43.8 vol.%. This change is similar to the large MXene particles, although the intensity of the inflection is less dependent on feature size, creating a parallel with the higher uniformity seen in the pure particle spray. Importantly, this inflection point tells us that this change cannot be accounted for simply because the total solution concentration was higher: only 28% more material was sprayed, yet the excess widths increased by 154 – 232% depending on the feature size. Turning to the unpatterned thickness, the film shows a greater initial slope, no indication of plateau behavior, and greater variability as the thickness increases. These characteristics indicate that this film is not in the SL regime, corroborating the hypothesis that a transition occurred due to percolation.

Finally, continuing this trend, from the ITO particles, we can see that the percolation threshold can be pushed even higher when using an even lower aspect ratio, 0D particle. At 40.6

vol%, the ITO still forms nanowires (**Figure 5b**). However, its lower unpatterned growth rate, combined with its EWs, which are within the range of 28 vol.% MXene EWs, indicate that these materials are still SL.

4.3 Upgraded commercial device

The device demonstrated in **Figure 5**, while not the first device created through ESD, is the first micropatterned device created by SLED and by any ESD without the use of (1) a near field (*i.e.*, photoresist) or far-field (*i.e.*, stencil) mask or (2) a near-field direct write (*i.e.*, electrohydrodynamic printing) approach, with the advantages of this discussed below. Despite this and the large increases in response, the supercapacitor device underperforms compared to similar devices in literature.[38] Surprisingly, this was not due to burning in air, as vacuum-annealed and argon-annealed devices did not surpass this performance, although the gaseous products of MC may be the cause. There appears to be a large voltage drop due to high resistance and possibly parasitic redox reactions. The resistance may result from residual carbon, which is expected to be around 10 - 20% for bulk MC.[39] Work from the Hersam group detailed how residual carbon from nitrocellulose improved graphene-based electronics.[40] However, it may have a detrimental effect here, due to the higher conductivity of MXene compared to reduced graphene oxide. Another option is that active material density is relatively low, and the porous MXene provides poor edge contact between flakes. Indeed, the specific performance might be greater for these structures. Further improvements in formulation and post-processing tuned for the materials involved may lead to better performance.

Despite some setbacks, the key innovation and novelty here is the scalability. Beginning with a device manufactured using well-established processes, we can rapidly functionalize the surface in ambient conditions in a matter of minutes, though binder removal requires some environmental control depending on the particle used. It should also be noted that SLED is agnostic to the conductive target and "conductive" includes materials with low conductivity such as biological material and hydrogels.[2, 26] This means that lower-quality electrodes could be upgraded in this way, such as those produced in ITO or by direct ink writing of metal inks. Furthermore, we remove the ink optimization and registry requirements of direct-write methods for targeting prepatterned electrodes, and we can functionalize multiple devices using a single sprayer through continuous manufacturing approaches, with further scaling achievable using multiple spray nozzles. Other work by our group has shown that SLED can be achieved with efficiency approaching 100%,[13] allowing for a low-waste fabrication route. Finally, MC removal occurs at a temperature polyimide can withstand, allowing for compatibility with flexible devices.

5 Conclusions

This work has demonstrated that conductive functional MXene particles can be sprayed in the self-limiting regime via compositing with a SLED carrier material. This capability was shown to be dependent on particle concentration, with distinct transitions observable in both the excess width of patterned grating and the growth rates of unpatterned films. Furthermore, the concentration at which these transitions occurred depended on the particle geometry, chemistry, and electrical properties. This work demonstrates the capabilities of SLED for manufacturing micron-scale devices. We see excellent agreement with our prior findings, which described the benefits of uniformity and fidelity that could be achieved with self-limiting materials on micro-patterned substrates.[3] Here, using SLED binder to create a green body, we patterned 50 μm features on an interdigitated electrode using the 28 vol.% sonicated MXene composite and produced a supercapacitor by burning off the binder. Although the MXene particles are sensitive to oxygen and we expect that residual carbon likely impacted device performance, these barriers do not exist for other particle systems,[40] and it may be possible to improve these results with cleaner burning polymers. Regardless, the ease with which we achieve porosity and the capability for 3D coatings (**Figure S7**) is unique in the context of printed nanoparticle inks. Overall, our high levels of control over nanoparticle sprays enable a vast field of designer coatings that can be delivered to high-resolution or topologically complex templates with a high level of control over nanoscale morphology.

Acknowledgments:

The authors acknowledge funding from the National Science Foundation through Awards 1911518 and 2019849. Additionally, J. P. S. and M. J. G. acknowledge funding through the Rutgers Mary W. Raisler Distinguished Teaching Chair. The authors would like to thank S. Rahman Pejman for conducting conductivity measurements and Rachel Vladimirsky for contributions to preliminary data.

Conflict of Interest:

M. J. G. and J. P. S. are cofounders of a recently incorporated company (Plumajet) that seeks to commercialize self-limiting electrospray deposition technology. No other authors have conflicts to declare.

Table of Contents:

Self-limiting electrospray deposition (SLED) uses trapped charge in a growing film to redirect incoming material and produce highly targeted and uniform sprays. Here, nanoparticles are added to sprays to functionalized pre-patterned electrodes and other devices. It was found that when the polymer binder content is optimized and particle percolation is prevented, self-limiting behavior is maintained, and unform patterning can be achieved.

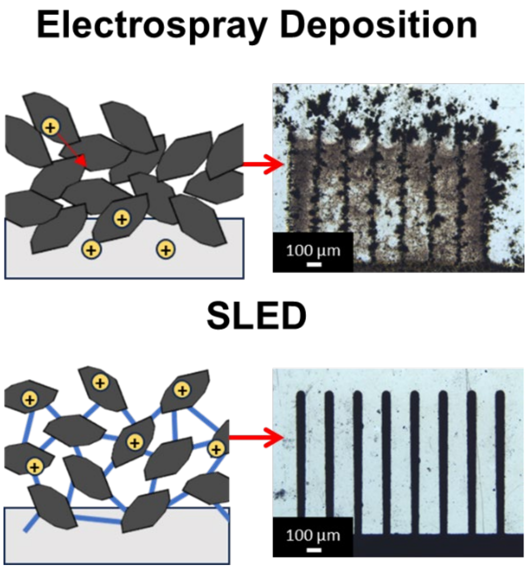

References

(1) Lei, L.; Kovacevich, D. A.; Nitzsche, M. P.; Ryu, J.; Al-Morzoki, K.; Rodriguez, G.; Klein, L. C.; Jitianu, A.; Singer, J. P. Obtaining thickness-limited electrospray deposition for 3D coating. *ACS Applied Materials & Interfaces* **2018**, *10* (13), 11175–11188. DOI: 10.7282/T31C213Q.

(2) Kovacevich, D. A.; Lei, L.; Han, D.; Kuznetsova, C.; Kooi, S. E.; Lee, H.; Singer, J. P. Self-limiting electrospray deposition for the surface modification of additively manufactured parts. *ACS Applied Materials & Interfaces* **2020**, *12* (18), 20901-20911. DOI: 10.1021/acsami.9b23544.

(3) Grzenda, M. J.; Atzampou, M.; Samateh, A.; Jitianu, A.; Zahn, J. D.; Singer, J. P. Microscale templating of materials across electrospray deposition regimes. *Coatings* **2023**, *13* (3), 599.

(4) Barrero, A.; Loscertales, I. G. Micro- and nanoparticle via capillary flows. *Annual Review of Fluid Mechanics* **2008**, *39*, 89-106. DOI: 10.1146/annurev.fluid.39.050905.110245.

(5) Zhang, S.; Kawakami, K. One-step preparation of chitosan solid nanoparticles by electrospray deposition. *International Journal of Pharmaceutics* **2010**, *397* (1), 211-217. DOI: https://doi.org/10.1016/j.ijpharm.2010.07.007.

(6) Lai, W.; Di, L.; Zhao, C.; Tian, Y.; Duan, Y.; Pan, Y.; Ye, D.; Jiang, L.; Guo, Y.; He, G. Electrospray deposition for electronic thin films on 3D freeform surfaces: From mechanisms to applications. *Advanced Materials Technologies* **2024**, 2400192.

(7) Sollami Delekta, S.; Smith, A. D.; Li, J.; Östling, M. Inkjet printed highly transparent and flexible graphene micro-supercapacitors. *Nanoscale* **2017**, *9* (21), 6998-7005. DOI: 10.1039/C7NR02204B.

(8) Li, J.; Unander, T.; López Cabezas, A.; Shao, B.; Liu, Z.; Feng, Y.; Bernales Forsberg, E.; Zhang, Z.-B.; Jõgi, I.; Gao, X.; et al. Ink-jet printed thin-film transistors with carbon nanotube channels shaped in long strips. *Journal of Applied Physics* **2011**, *109* (8), 084915. DOI: 10.1063/1.3569842.

(9) Fuller, S. B.; Wilhelm, E. J.; Jacobson, J. M. Ink-jet printed nanoparticle microelectromechanical systems. *Journal of Microelectromechanical Systems* **2002**, *11* (1), 54-60. DOI: 10.1109/84.982863.
(10) Walden, P.; Kneer, J.; Knobelspies, S.; Kronast, W.; Mescheder, U.; Palzer, S. Micromachined hotplate platform for the investigation of ink-jet printed, functionalized metal oxide nanoparticles. *Journal of Microelectromechanical Systems* **2015**, *24* (5), 1384-1390. DOI: 10.1109/JMEMS.2015.2399696.
(11) Kukkola, J.; Mohl, M.; Leino, A.-R.; Tóth, G.; Wu, M.-C.; Shchukarev, A.; Popov, A.; Mikkola, J.-P.; Lauri, J.; Riihimäki, M.; et al. Inkjet-printed gas sensors: metal decorated WO3 nanoparticles and their gas sensing properties. *Journal of Materials Chemistry* **2012**, *22* (34), 17878. DOI: 10.1039/c2jm32499g.
(12) Khan, Y.; Thielens, A.; Muin, S.; Ting, J.; Baumbauer, C.; Arias, A. C. A new frontier of printed electronics: flexible hybrid electronics. *Advanced Materials* **2020**, *32* (15), 1905279. DOI: 10.1002/adma.201905279.
(13) Park, S. H.; Lei, L.; D'Souza, D.; Zipkin, R.; DiMartini, E. T.; Atzampou, M.; Lallow, E. O.; Shan, J. W.; Zahn, J. D.; Shreiber, D. I.; et al. Efficient electrospray deposition of surfaces smaller than the spray plume. *Nature Communications* **2023**, *14* (1), 4896. DOI: 10.1038/s41467-023-40638-7.
(14) Hwang, D.; Lee, H.; Jang, S.-Y.; Jo, S. M.; Kim, D.; Seo, Y.; Kim, D. Y. Electrospray preparation of hierarchically-structured mesoporous TiO2 spheres for use in highly efficient dye-sensitized solar cells. *ACS Applied Materials & Interfaces* **2011**, *3* (7), 2719-2725. DOI: 10.1021/am200517v.
(15) García-Farrera, B.; Velásquez-García, L. F. Ultrathin Ceramic Piezoelectric Films via Room-Temperature Electrospray Deposition of ZnO Nanoparticles for Printed GHz Devices. *ACS Applied Materials & Interfaces* **2019**, *11* (32), 29167-29176. DOI: 10.1021/acsami.9b09563.
(16) Mustafa, M.; Awais, M. N.; Pooniah, G.; Choi, K. H.; Ko, J.; Doh, Y. H. Electrospray deposition of a graphene-oxide thin film, its characterization and investigation of its resistive switching performance. *Journal of the Korean Physical Society* **2012**, *61* (3), 470-475. DOI: 10.3938/jkps.61.470.
(17) Kim, J. W.; Yamagata, Y.; Kim, B. J.; Higuchi, T. Direct and dry micro-patterning of nano-particles by electrospray deposition through a micro-stencil mask. *Journal of Micromechanics and Microengineering* **2009**, *19* (2), 025021. DOI: 10.1088/0960-1317/19/2/025021.
(18) Higashi, K.; Uchida, K.; Hotta, A.; Hishida, K.; Miki, N. Micropatterning of silica nanoparticles by electrospray deposition through a stencil mask. *Journal of Laboratory Automation* **2014**, *19* (1), 75-81. DOI: 10.1177/2211068213495205.
(19) Khan, S.; Doh, Y. H.; Khan, A.; Rahman, A.; Choi, K. H.; Kim, D. S. Direct patterning and electrospray deposition through EHD for fabrication of printed thin film transistors. *Current Applied Physics* **2011**, *11* (1), S271-S279. DOI: 10.1016/j.cap.2010.11.044.
(20) Zhu, Y.; Chiarot, P. R. Directed assembly of nanomaterials using electrospray deposition and substrate-level patterning. *Powder Technol.* **2020**, *364*, 845-850. DOI: https://doi.org/10.1016/j.powtec.2020.01.066.
(21) Li, X.; Zhang, Z.; Peng, Z.; Yan, X.; Hong, Y.; Liu, S.; Lin, W.; Shan, Y.; Wang, Y.; Yang, Z. Fast and versatile electrostatic disc microprinting for piezoelectric elements. *Nature communications* **2023**, *14* (1), 6488-6488. DOI: 10.1038/s41467-023-42159-9.

(22) Kingsley, B. J.; Pawliczak, E. E.; Hurley, T. R.; Chiarot, P. R. Electrospray printing of polyimide films using passive material focusing. *ACS Applied Polymer Materials* **2021**, *3* (12), 6274-6284. DOI: 10.1021/acsapm.1c01073.
(23) Nan, C. W.; Shen, Y.; Ma, J. Physical properties of composites near percolation. *Annual Review of Materials Research* **2010**, *40* (1), 131-151. DOI: 10.1146/annurev-matsci-070909-104529.
(24) Zhu, Y.; Chiarot, P. R. Structure of nanoparticle aggregate films built using pulsed-mode electrospray atomization. *JMatS* **2019**, *54* (8), 6122-6139. DOI: 10.1007/s10853-019-03349-3.
(25) Green-Warren, R. A.; Bontoux, L.; McAllister, N. M.; Kovacevich, D. A.; Shaikh, A.; Kuznetsova, C.; Tenorio, M.; Lei, L.; Pelegri, A. A.; Singer, J. P. Determining the Self-Limiting Electrospray Deposition Compositional Limits for Mechanically Tunable Polymer Composites. *ACS Applied Polymer Materials* **2022**, *4* (5), 3511-3519. DOI: 10.1021/acsapm.2c00106.
(26) Lei, L.; Chen, S.; Nachtigal, C. J.; Moy, T. F.; Yong, X.; Singer, J. P. Homogeneous gelation leads to nanowire forests in the transition between electrospray and electrospinning. *Materials Horizons* **2020**, *7* (10), 2643 - 2650. DOI: 10.1039/D0MH00872A.
(27) Blisko, J.; Grzenda, M. J.; Vladimirsky, R. M.; Shuck, C. E.; Singer, J. P.; Yong, X. Controlling morphology in electrosprayed methylcellulose nanowires via nanoparticle addition: coarse-grained modeling and experiments. *Nanoscale* **2022**, (14), 17985-17994.
(28) Kovacevich, D. A.; Lei, L.; Han, D.; Kuznetsova, C.; Kooi, S. E.; Lee, H.; Singer, J. P. Self-Limiting Electrospray Deposition for the Surface Modification of Additively Manufactured Parts. *ACS Appl Mater Interfaces* **2020**, *12* (18), 20901-20911. DOI: 10.1021/acsami.9b23544.
(29) Shuck, C. E.; Ventura-Martinez, K.; Goad, A.; Uzun, S.; Shekhirev, M.; Gogotsi, Y. Safe synthesis of MAX and MXene: guidelines to reduce risk during synthesis. *Journal of Chemical Health & Safety (Online)* **2021**, *28* (5), 326-338. DOI: 10.1021/acs.chas.1c00051.
(30) McAllister, N. M.; Green-Warren, R. A.; Arkhipov, M.; Lee, J. H.; Pelegri, A. A.; Singer, J. P. Non-destructive thickness measurement of optically scattering polymer films using image processing. *Engineering Reports* **2023**, e12830. DOI: 10.1002/eng2.12830.
(31) Lipatov, A.; Goad, A.; Loes, M. J.; Vorobeva, N. S.; Abourahma, J.; Gogotsi, Y.; Sinitskii, A. High electrical conductivity and breakdown current density of individual monolayer Ti3C2Tx MXene flakes. *Matter* **2021**, *4* (4), 1413-1427.
(32) Granqvist, C. G.; Hultåker, A. Transparent and conducting ITO films: New developments and applications. *Thin Solid Films* **2002**, *411* (1), 1-5. DOI: https://doi.org/10.1016/S0040-6090(02)00163-3.
(33) Haynes, W. M. Electrical resistivity of pure metals. In *CRC handbook of chemistry and physics*, CRC press, 2016.
(34) Bartzsch, H.; Glöß, D.; Böcher, B.; Frach, P.; Goedicke, K. Properties of SiO2 and Al2O3 films for electrical insulation applications deposited by reactive pulse magnetron sputtering. *Surface and Coatings Technology* **2003**, *174*, 774-778.
(35) Liu, J.; Hurt, R. H. Ion Release Kinetics and Particle Persistence in Aqueous Nano-Silver Colloids. *Environmental Science & Technology* **2010**, *44* (6), 2169-2175. DOI: 10.1021/es9035557.
(36) Boxley, C. J.; White, H. S.; Gardner, C. E.; Macpherson, J. V. Nanoscale Imaging of the Electronic Conductivity of the Native Oxide Film on Titanium Using Conducting Atomic Force Microscopy. *The Journal of Physical Chemistry B* **2003**, *107* (36), 9677-9680. DOI: 10.1021/jp034874u.

(37) Balberg, I. Excluded-volume explanation of Archie's law. *Physical Review. B, Condensed Matter* **1986**, *33* (5), 3618-3620. DOI: 10.1103/PhysRevB.33.3618.
(38) Lei, Y.; Zhao, W.; Zhu, Y.; Buttner, U.; Dong, X.; Alshareef, H. N. Three-dimensional Ti3C2Tx MXene-prussian blue hybrid microsupercapacitors by water lift-off lithography. *ACS Nano* **2022**, *16* (2), 1974-1985. DOI: 10.1021/acsnano.1c06552.
(39) Rodrigues Filho, G.; de Assunção, R. M.; Vieira, J. G.; Meireles, C. d. S.; Cerqueira, D. A.; da Silva Barud, H.; Ribeiro, S. J.; Messaddeq, Y. Characterization of methylcellulose produced from sugar cane bagasse cellulose: Crystallinity and thermal properties. *Polymer Degradation and Stability* **2007**, *92* (2), 205-210.
(40) Secor, E. B.; Gao, T. Z.; Islam, A. E.; Rao, R.; Wallace, S. G.; Zhu, J.; Putz, K. W.; Maruyama, B.; Hersam, M. C. Enhanced conductivity, adhesion, and environmental stability of printed graphene inks with nitrocellulose. *Chemistry of Materials* **2017**, *29* (5), 2332-2340. DOI: 10.1021/acs.chemmater.7b00029.

Supplementary Information

Microscale Templating of Particles using Self-Limiting Electrospray Deposition

Michael J. Grzenda[1], Jouan Yu[1], Maria Atzampou[2], Christopher E. Shuck[3], Yury Gogotsi[4], Jeffrey D. Zahn[2], Jonathan P. Singer[1]

1. Department of Mechanical and Aerospace Engineering, Rutgers University, Piscataway, New Jersey 08854, USA. E-mail: jonathan.singer@rutgers.edu
2. Department of Biomedical Engineering, Rutgers University, Piscataway, NJ 08854, USA
3. Department of Chemistry and Chemical Biology, Rutgers University, Piscataway, NJ 08854, USA
4. A.J. Drexel Nanomaterials Institute, and Department of Materials Science and Engineering, Drexel University, Philadelphia, Pennsylvania 19104, USA

Excess width of dilute vs. non-dilute small MXene

Comparing the concentrated vs dilute small MXene sprays, we see the 0.25 wt.% MC composites show greater excess widths than their 1 wt.% MC counterparts when the MC/MXene ratio is matched. We also see that for the 28 vol.% composition, the same trend holds for the unpatented film thickness across time intervals. This is likely the result of several factors, and more definitive answers will require simulation. For one, changing the concentration does impact the spray morphology. For example, when depositing only nanoparticles, it has been reported that high-concentration sprays produce spherical agglomerates, while low concentrations lead to irregular agglomerates.[24] Spray morphology is strongly dependent on the interaction of viscous forces and surface tension during deposition, and these can vary greatly when the ratio of solids to solvent is altered. One can also imagine that having less material per droplet will reduce the overall "grain" size. For pure MC, our past report observed that 0.25 wt.% MC will deliver thinner wires than 1 wt.% MC.[26] It is also known that charge relaxation occurs over time in air leading to a slight increase in material deposition for longer sprays. However, the pure 0.25 wt.% MC has excess widths that are within the error of the pure 1 wt.% MC spray, indicating charge relaxation is not the only factor to consider for the composites. One possibility is that increased surface area from the thicker composite layer allows for more charge dissipation in air, creating a synergistic effect. Another is that the MC may be less able to encapsulate the particles at 0.25 wt.% solution concentration.

Impact of feature size on excess width

As mentioned, prior work has shown that on the test patterns used here, SLED sprays showed less variation in thickness across feature sizes compared to non-SLED sprays. In this work, the same is true for the large MXene flakes. At 4.7 vol.%, the average EWs ranges from 31.32 - 46.10 μm, while for 8.9 vol.%, the range has expanded to 69.75 - 123.97 μm with smaller features experiencing greater growth in both cases. However, for small/dilute MXene, the trend is less obvious. Here, the range is 165.24 - 194.3 μm, with the 120 μm feature actually showing the largest EW. This trend mirrors the qualitative assessment of the non-composite sprays, where the small MXene flakes were more uniform than their larger counterparts. This is likely the result of both denser packing and more interfaces interrupting the flow of charge for the smaller particles. For silica, we do see a slight trend. At 31.5 vol.%, the range is from 8.16 – 15.33 μm, while at 78.6 vol.%, this range has increased to 19.98 – 39.8 vol.%. Although small, the difference in slope for each feature is apparent in **Figure S3**. This gives further evidence to the hypothesis that 78.6 vol.% silica is in an intermediate regime.

Table S1. Comparison of film thickness on patterned and unpatterned substrates. Excess width has been divided by two to give the growth on a single feature edge.

Solution	Substrate	Time (hr)	Thickness (µm)	Std Dev
Pure MC	Flat	2	4.75	0.25
	Flat	3	9.04	0.75
	20 µm feature	2	8.87	0.72
	240 µm feature	2	5.71	0.76
28 vol.% Mxene (non-dilute)	Flat	2	8.09	1.83
	Flat	3	10.98	1.41
	20 µm feature	2	15.63	0.75
	240 µm feature	2	10.67	2.98
43% Mxene (dilute)	Flat	8	88.48	7.32
	20 µm feature	8	93.52	6.32
	240 µm feature	8	82.62	5.39

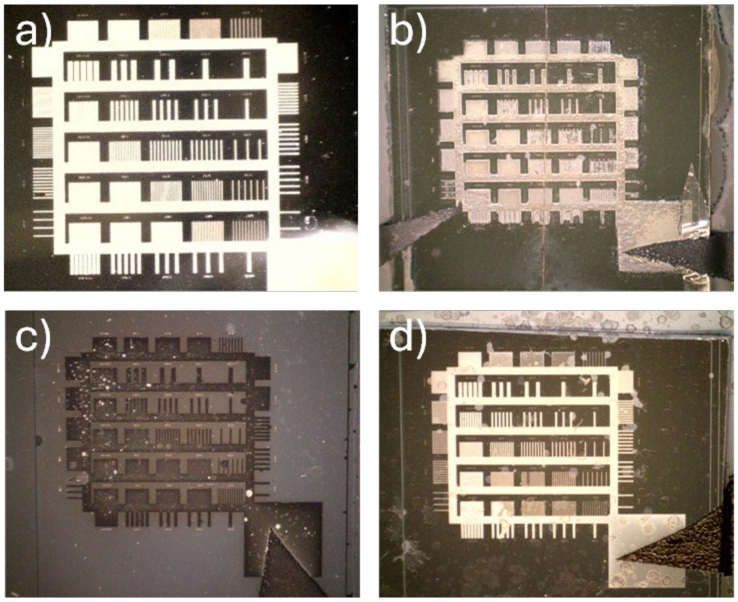

Figure S1. Images of the entire test pattern for non-composite sprays of (a) MC, (b) large MXene flakes, (c) small MXene flakes, and (d) ITO.

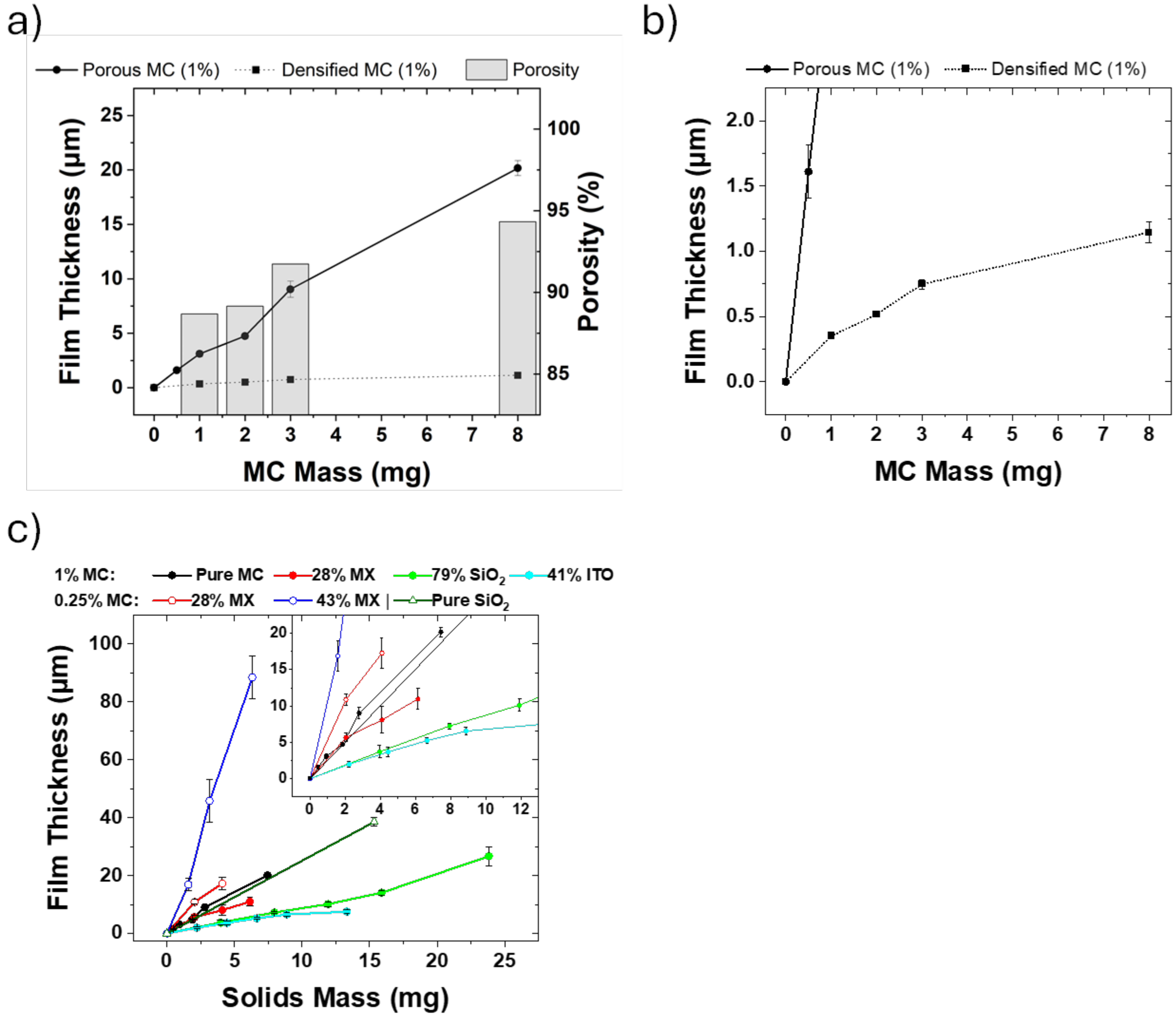

Figure S2. Unpatterned thickness of the as sprayed MC (porous) compared to its densified thickness (a, b). The MC was densified by cooling the sprayed wafers in a freezer and allowing condensation to smooth the films via solvent absorption. (c) Unpatterned thickness of all measured materials.

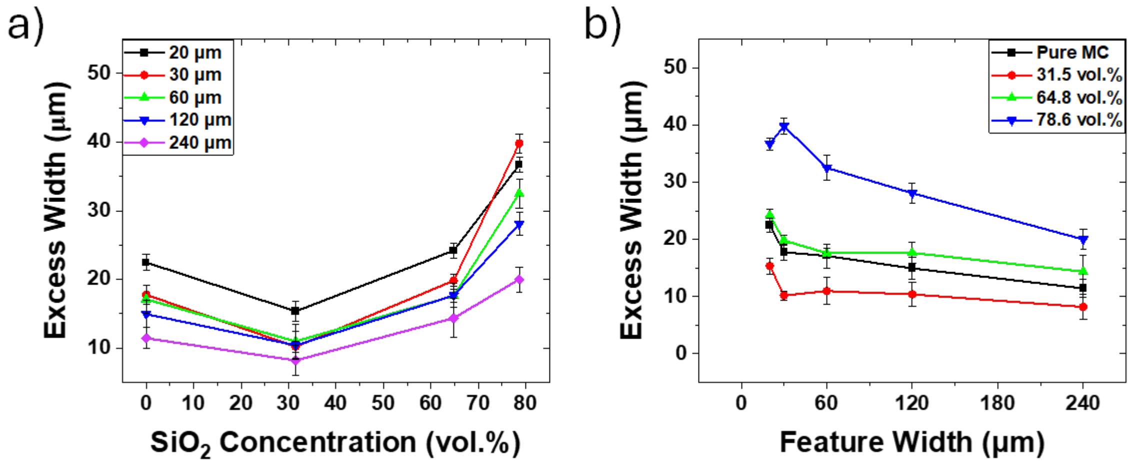

Figure S3. Excess width of silica particles across (a) concentration and (b) feature width sprayed from a 1 wt.% MC solution.

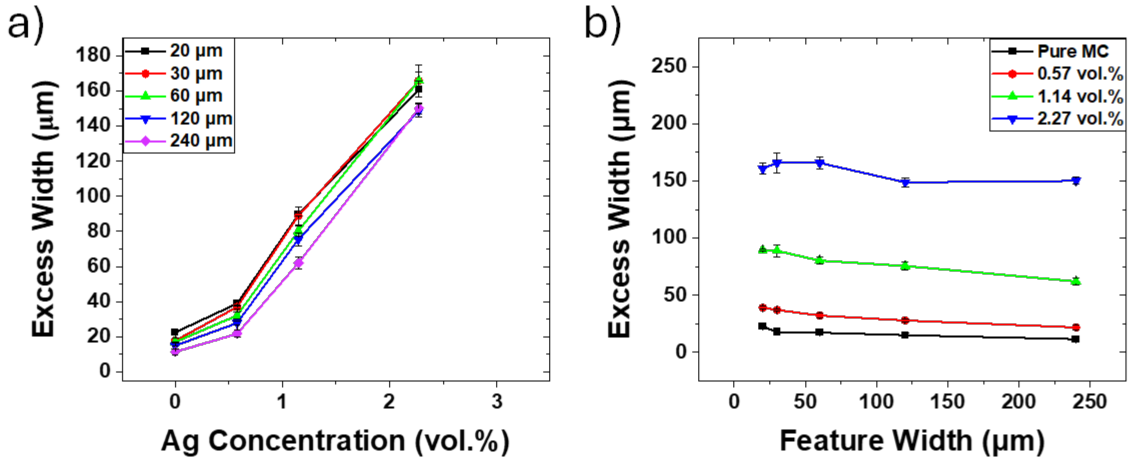

Figure S4. Excess width of silver particles across (a) concentration and (b) feature width sprayed from a 1 wt.% MC solution.

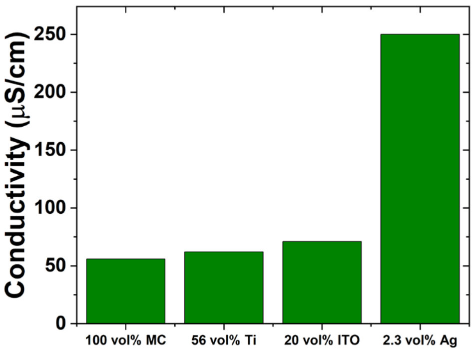

Figure S5. Electrical conductivity of select spray solutions as measured by an Oakton Con 550 conductivity meter.

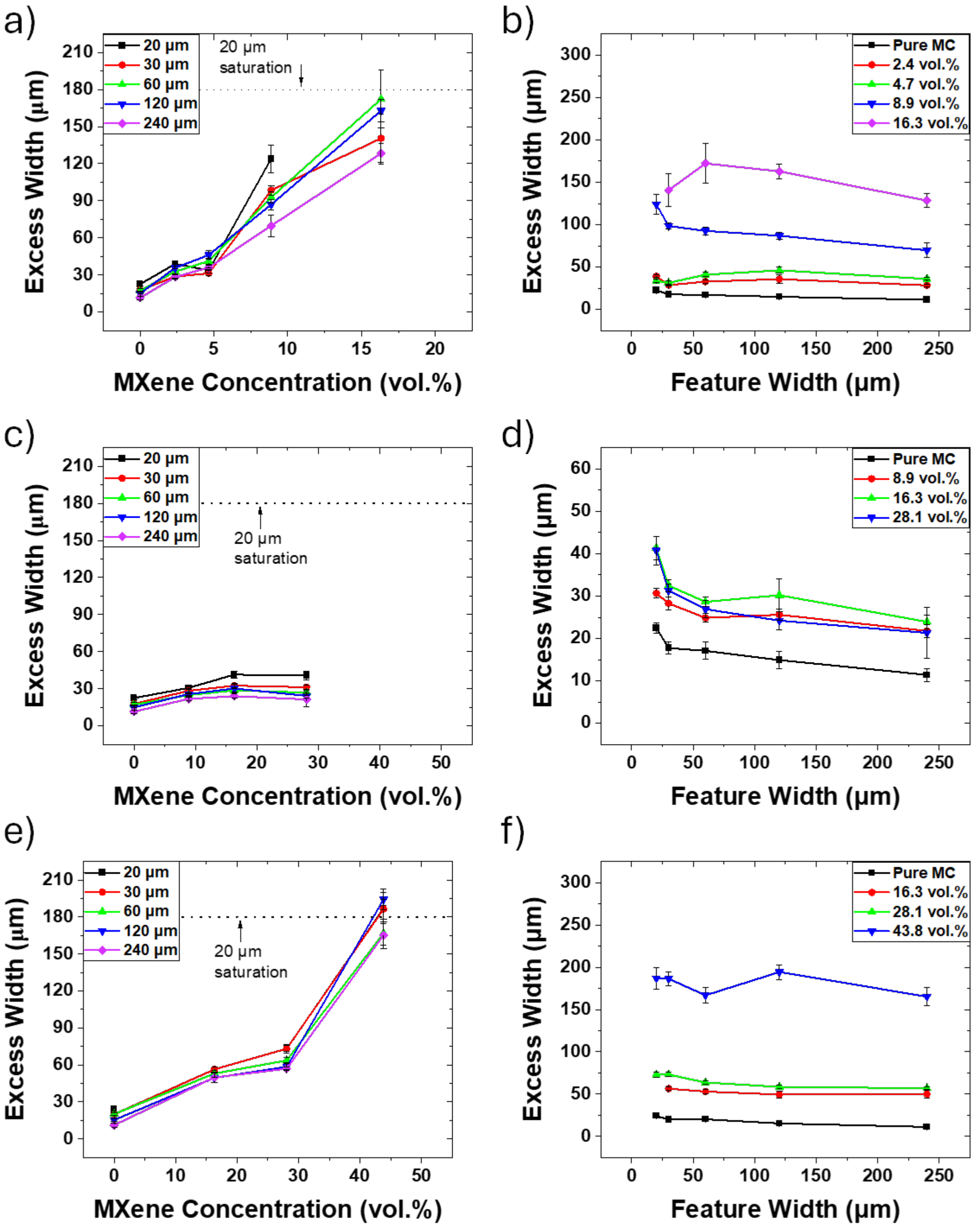

Figure S6. Excess width of large MXene flakes across (a) concentration and (b) feature width sprayed from a 1 wt.% MC solution. Small MXene flakes sprayed form a “concentrated” 1 wt.% MC solution (c & d) and small MXene flakes sprayed from a “dilute” 0.25 wt.% MC solution (c & d respectively).

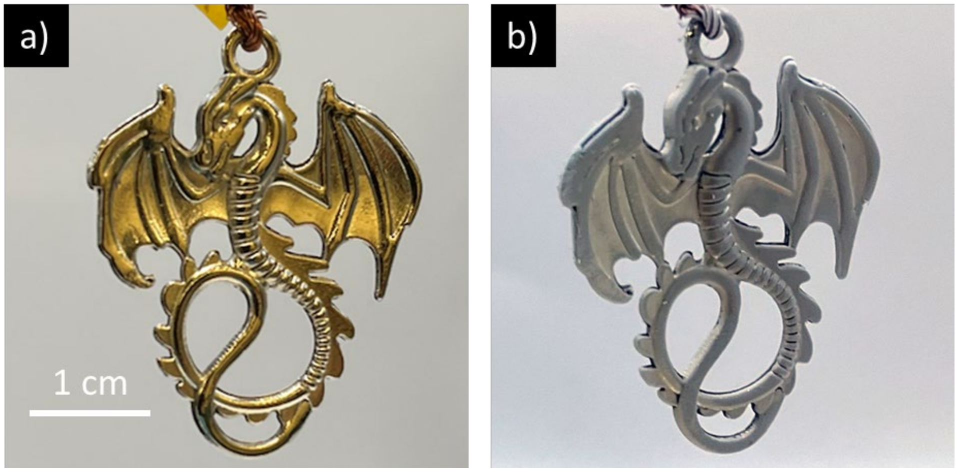

Figure S7. Zinc alloy figurine before (a) and after (b) coating with 20 vol% ITO deposited from 1 wt% MC solution for one hour. Other parameters: 7.0 kV spray voltage, 2.1 kV stabilizing ring voltage, 0.4 mL/h, room temperature, 4 cm closest spray distance. While the coating conforms to the 3D surface of the object, it should be noted that regions with patina (particularly the black ridges) are masked and, thereby, selectively uncoated.